

De Haas–van Alphen effect in graphene

Juuso Manninen,^{1,2,*} Antti Laitinen,^{1,3,*} Francesco Massel,^{4,5} and Pertti Hakonen^{1,2,†}

¹*Low Temperature Laboratory, Department of Applied Physics,
Aalto University, PO Box 15100, FI-00076 AALTO, Finland*

²*QTF Centre of Excellence, Department of Applied Physics,
Aalto University, PO Box 15100, FI-00076 AALTO, Finland*

³*Department of Physics, Harvard University, Cambridge, MA 02138, USA*

⁴*Department of Physics, Nanoscience Center,
University of Jyväskylä, FIN 40014, Finland*

⁵*Department of Science and Industry Systems,
University of South-Eastern Norway, PO Box 235, Kongsberg, Norway*

arXiv:2112.01102v1 [cond-mat.mes-hall] 2 Dec 2021

Abstract

In our work, we study the dynamics of a graphene Corbino disk supported by a gold mechanical resonator in the presence of a magnetic field. We demonstrate here that our graphene/gold mechanical structure exhibits a nontrivial resonance frequency dependence on the applied magnetic field, showing how this feature is indicative of the de Haas–van Alphen effect in the graphene Corbino disk. Our findings are the first evidence of dHvA effect for massless Dirac fermions. By relying on the mechanical resonances of the Au structure, our detection scheme is essentially independent of the material considered and can be applied for dHvA measurements on any conducting 2D material. In particular, the scheme is expected to be an important tool in studies of centrosymmetric transition metal dichalcogenides (TMDs) crystals, shedding new light on hidden magnetization and interaction effects.

INTRODUCTION

As theoretically shown by Landau and Peierls in the 1930s [1, 2], the de Haas–van Alphen (dHvA) effect consists of a periodic oscillation of the magnetization (and the magnetic susceptibility) as a function of the magnetic field. Along with other magnetic-field-induced phenomena, such as the Shubnikov de Haas (SdH) conductance oscillations, the quantum Hall effect, and quantum capacitance oscillations, the origin of the dHvA effect is traced back to the modification of the electronic spectrum in the presence of a magnetic field. Since in this case electronic motion becomes quantized due to the formation of Landau levels, which are ultimately responsible for the non-trivial properties of the considered electronic system, it is quite natural that the dHvA effect has served as the central probe in studies of the shape of the Fermi surface in normal metals.

Besides investigations of the dHvA effect in conventional materials, magnetic properties of two-dimensional (2D) materials have been investigated actively [3, 4]. Unlike the 3D case, where the field dependence of the magnetization is described by the classical 3D Landau-Kosevich formula, for 2D samples the magnetization shows a characteristic sawtooth pattern both for massive and massless Dirac fermions [5]. On the experimental side, in 2D the dHvA effect was first observed by Eisenstein et al. in 1985 [6] in a 2D electron gas (2DEG), while a clear sawtooth pattern for the magnetization vs. inverse magnetic field predicted in [2] was resolved about ten years later [7]. Focusing on detection techniques of magnetic properties

based on mechanical motion, surface acoustic waves (SAW) have extensively been used for imaging of integer and fractional quantum Hall states (QH) [8] in conventional GaAs 2DEG systems. In SAW-based techniques, mechanical motion is coupled to the electron system due to piezoelectric response of GaAs, and variation in the compressibility of the electron system modulates attenuation and sound velocity in the material. Apart from SAW resonances, QH states in a 2DEG have also been investigated through curling [9], cantilever [10, 11], and torsional modes [6].

For two-dimensional materials, such as graphene and transition metal dichalcogenides (TMDs), while SdH conductance oscillations have been reported [12–14] in graphene, experiments have not yet revealed the dHvA effect. This is the focus of our work: we report here, for the first time, a dHvA measurement for a graphene membrane in a Corbino geometry coupled to a gold (Au) mechanical resonator. This configuration allows us to exploit the possibilities offered by suspended resonators in addressing the magnetic properties of Dirac fermions in graphene and, in principle, the carrier-dependent magnetic behavior in other 2D materials.

While previous experiments on suspended graphene mechanical resonators have focused on displaying the periodic variation of quantum capacitance as a function of magnetic field B in the integer QH regime [15, 16], in our work, we extend such principle, showing how it is possible to perform a mechanical readout not only of the quantum capacitance, but also of the magnetic susceptibility of the graphene sheet. This can be done evaluating the explicit functional dependence of the quantum capacitance on the magnetic susceptibility.

The basic measurement principle of our experiment is illustrated schematically in Fig. 1. Our experiments were carried out on two devices: B2 and B1.5. Device B2 consists of *two Au beams*, one graphene Corbino disk, and a back gate to which a voltage V_g is applied, controlling the charge density n on the graphene disk. The Corbino disk couples the two Au beams together mechanically; the parallel Au beams are located at different heights, about 150 nm apart, supported by a bend in the center of the upper Au beam (Fig. 1a,c). Device B1.5 consists of *one and a half Au beams*: the top Au beam has been replaced by a gold cantilever in it (Fig. 1b). An electrical current can be passed through between the terminal source and drain, marked in Fig. 1b,c by S and D, respectively. The Au beams and the cantilever have nearly the same bending rigidity. This leads to the appearance of mechanical resonance frequencies between 10 and 100 MHz for both devices, basically governed by the

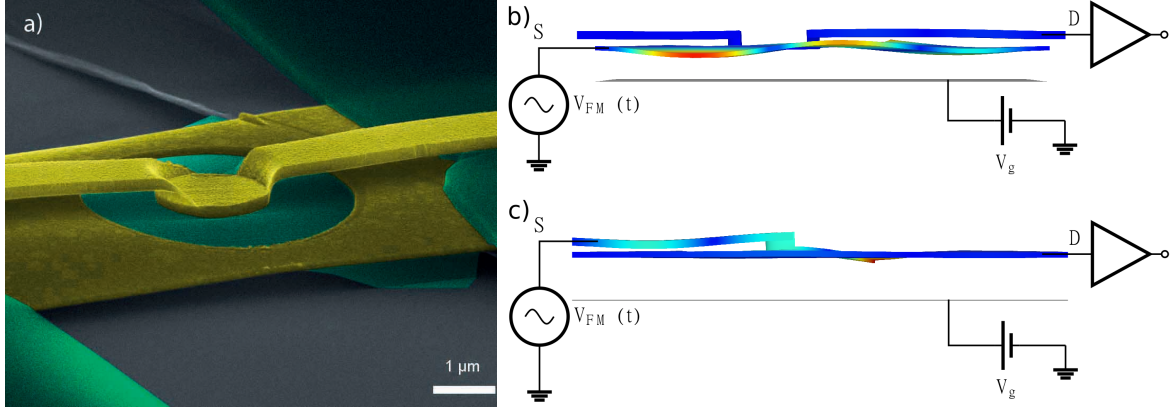


FIG. 1. **Sample structure and key mechanical modes.** a) SEM image of the measured device B2. The ring shaped graphene colored green, Au parts appear as yellow, polymer support as dark green, and the substrate is gray. The length of the lower gold beam amounts $8 \mu\text{m}$. Schematic of our measurement method for the device b) B2 and c) B1.5 consisting of two Au electrodes, one graphene Corbino disk, a back gate voltage V_g , and the frequency modulation voltage V_{FM} . Mode shapes (not in scale) obtained from FEM simulations of the respective devices utilized in this study are depicted with a color gradient highlighting the physical displacement.

gold structures, with the dynamics of the graphene membrane being dictated by the motion of the graphene/gold boundary conditions.

Owing to the mechanical motion of the graphene membrane, the charge distribution within the Corbino disk will be affected, altering the capacitive forces at play and, consequently, the mechanical resonances of the combined structure in the presence of an external biasing voltages and/or magnetic fields. In our devices, we can picture the gold oscillator acting as a mechanical detector of the magnetic (magnetization, magnetic susceptibility) and electronic (quantum capacitance) properties of the graphene disk. Our approach is along the lines of cantilever sensing [11], but differs fully in the sense that our method allows us to investigate different materials independent of the probing mechanical cantilever (in our case the Au structure) and thus the method is applicable to any 2D material, many of which can be fabricated into mechanical resonators [17, 18]. The idea of using mechanical motion to measure the magnetic properties of a graphene membrane introduced here can be considered as a part of the emerging field of sensing with 2D mechanical resonators [19].

BASIC EXPERIMENTAL CHARACTERISTICS

Owing to the difference in effective mass between the Au and graphene portions of the devices, two basic types of resonances were observed in our samples: (low-frequency 10-40 MHz) combined gold-graphene modes (“Au mode”) and (high-frequency $\gtrsim 90$ MHz) pure graphene resonances in the Corbino disk [20]. Due to the mechanical properties of the Au beams, for combined gold-graphene modes, there is a wider range of driving fields for which the linear detection of the quantum Hall states in graphene is possible in comparison with pure graphene modes. For these modes, the linear regime is limited to oscillation amplitudes around 100 pm [21]. For this reason, and for the “material independence” of Au modes, in the following we focus on the latter ones.

The quality of the investigated graphene disks with appreciable built-in strain was assessed by measuring the Landau fan diagram, $G(V_g, B)$, which is illustrated in Fig. 2a for sample B2 at $n = 4.3 \cdot 10^{11} \text{ cm}^{-2}$. The dark regions denote large resistance that correspond to hopping conductance along localized levels within gapped QH states. A full set of integer QH states becomes visible at fields $B \geq 0.5 \text{ T}$, while the fractional QH state $\nu = 1/3$ appears starting from $B \approx 3 \text{ T}$, similar to works in Refs. [22, 23].

The mechanical resonance properties of the samples were investigated using the FM mixing technique [24, 25], which was employed due to the clear-cut form of the mixing signal, exhibiting a sharp and consistent three-lobed peak structure, see Fig. 2b. Furthermore, both the conductance and the phase of the mixing current I_{mix} at mechanical the resonance were found to reflect the non-trivial B dependence of the electronic properties (see Fig. 2c): the local minima in G coincide with the upwards phase flips in I_{mix} caused by the change of sign of the derivative dG/dV_g across the gapped QH states. Thus, the phase flips in I_{mix} can be employed as sensitive detectors of the QH states in suspended graphene, and a Landau level sequence up to $\nu = 34$ can be resolved in Fig. 2c.

FORCES ACTING ON THE RESONATOR

Our graphene/gold mechanical resonator can be described as a capacitor with one movable plate coupled to an external voltage source. In addition to the conventional electromagnetic field energy between the capacitor plates, the system exhibits a contribution to its total

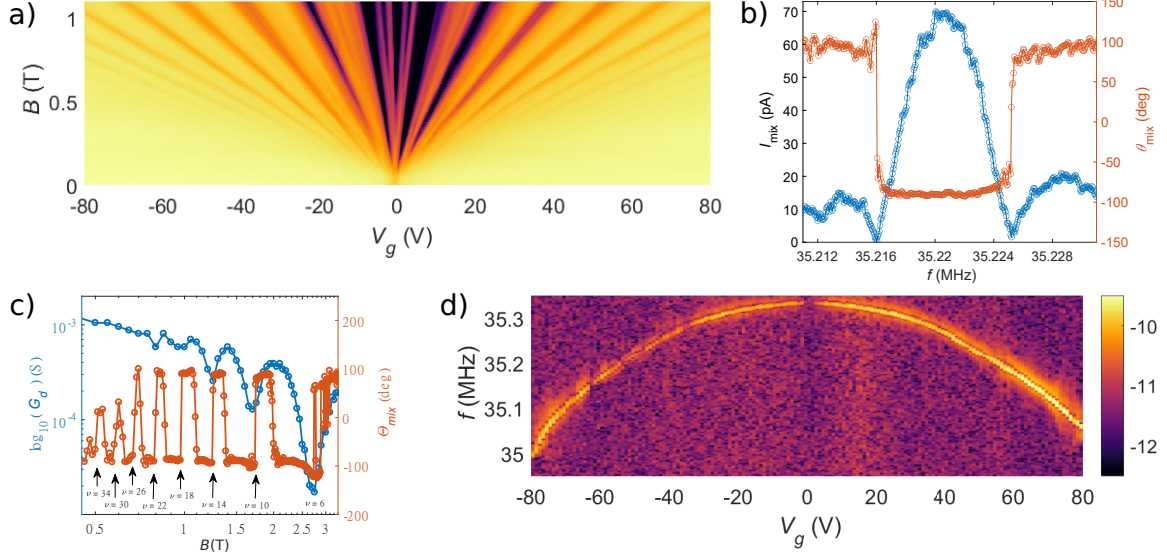


FIG. 2. **Characteristics of the suspended graphene Corbino disk B2.** a) Landau fan diagram over the gate voltage V_g vs. the magnetic field B plane, measured at $V_g = 60$ V ($n = 4.3 \cdot 10^{11} \text{ cm}^{-2}$). b) Mixing current I_{mix} and its phase of the 35 MHz resonance in zero magnetic field. c) Logarithm of conductance and the mixing current phase at resonance maximum as a function of magnetic field. d) V_g dependence of the logarithm of mixing current $\log_{10}(I_{\text{mix}})$ of the 35 MHz resonance.

energy deriving from the finite density of states (DOS) of graphene. In other terms, the external voltage V_g provides the external work required to build up the field between the capacitor plates, as in conventional capacitors, and, concomitantly, it is needed to overcome the extra energy associated with the finite DOS of graphene.

Such energy contribution leads to a reduction of the force between the plates of the movable capacitor

$$F = \frac{1}{2} C'_g \left(V_g - \frac{\mu}{e} \right)^2, \quad (1)$$

where V_g is the external applied voltage, μ the graphene chemical potential, C_g the (position-dependent) geometric capacitance of the structure, and C'_g its derivative with respect to the displacement of the graphene/gold electrode (see Supplementary Information). This formula fits well the measured gate dependence of the lower Au beam resonance presented in Fig. 2d.

In the presence of an external magnetic field, the resonant frequencies of our structures

f_n exhibit a nontrivial dependence on B reflecting the emergence of Landau levels in the spectrum of graphene. Along the lines of Ref. [16], we first express this frequency change in terms of quantum capacitive effects

$$\Delta f_n \doteq f_{B,n} - f_{B=0,n} = -\frac{\partial f_{0,n}}{\partial V} \left[\frac{\Delta\mu}{e} + C_g V_g \Delta \frac{1}{C_q} \right] + \frac{f_{0,n}}{2k_{0,n}} (C'_g V_g)^2 \Delta \left(\frac{1}{C_q} \right), \quad (2)$$

where $\partial f_{0,n}/\partial V$ is the $B = 0$ resonant frequency tunability with the gate voltage due to tensioning effects, $C_q = e^2 \partial n / \partial \mu$ is the graphene quantum capacitance, and $k_{0,n} = 4\pi^2 f_{0,n}^2 \rho$ is the effective elastic constant of mode n at $B = 0$ (see Supplementary Information). We note here that, due to the large effective elastic constant related to the density of gold taking part in the mechanical motion, in our setup the last term of Eq. (2) is negligible, leading to the appearance of local minima in the magnetic field dependence of f_n .

QUANTUM CAPACITANCE AND DE HAAS–VAN ALPHEN EFFECT IN GRAPHENE

Central to our analysis is the notion that it is possible to establish a direct relation between the graphene quantum capacitance C_q [26, 27] and the magnetic susceptibility χ_m . This correspondence allows us to relate the frequency shifts described in Eq. (2) to the magnetic susceptibility shifts and therefore consider Δf_n as a reliable measure of the dHvA effect.

As mentioned in relation to the force acting on the graphene/gold resonator given in Eq. (1), the properties of the whole system (moveable capacitor + graphene disk) can be derived from the relevant thermodynamic potential. In our case, given the $\bar{\mu} \doteq eV_g = \text{const}$ constraint, we consider the grand canonical potential $\Omega(\bar{\mu}, B)$, where the electrochemical potential $\bar{\mu} = eV_g$ is the global control parameter. From this perspective, μ is an energy contribution associated with the finite DOS of graphene and thus does not represent an independent control parameter and will therefore, in general, depend on the external magnetic field.

If we now confine ourselves to the analysis of the graphene sheet, i.e. we exclude the field between resonator and backgate from the definition of the system, we can assume that the independent control parameter is μ . This allows us to write the thermodynamic potential associated with the Corbino disk as $\Omega_{\text{disk}}(\mu, B) = \Omega_0(\mu) + \Omega_{\text{osc}}(\mu, B)$. The oscillatory

dependence on B is a direct consequence of the appearance of Landau levels in the energy spectrum [2, 28, 29]. From Ω_{osc} , it is possible to calculate the oscillating part of the magnetic susceptibility $\chi_{\text{m,osc}}$

$$\chi_{\text{m,osc}} = -\frac{Ne\mu}{4\pi\hbar B} \frac{\left(\mu^2 - \frac{\gamma^2}{4}\right) \left\{ e^{-2\pi\gamma\mu/\hbar\omega_{\text{D}}} - \cos \left[\frac{2\pi}{(\hbar\omega_{\text{D}})^2} \left(\mu^2 - \frac{\gamma^2}{4}\right) \right] \right\} + \gamma\mu \sin \left[\frac{2\pi}{(\hbar\omega_{\text{D}})^2} \left(\mu^2 - \frac{\gamma^2}{4}\right) \right]}{(\hbar\omega_{\text{D}})^2 \left\{ \cosh \left[\frac{2\pi\gamma\mu}{(\hbar\omega_{\text{D}})^2} \right] - \cos \left[\frac{2\pi}{(\hbar\omega_{\text{D}})^2} \left(\mu^2 - \frac{\gamma^2}{4}\right) \right] \right\}} \quad (3)$$

with N as the spin degeneracy factor, $\omega_{\text{D}} = \sqrt{2eB/\hbar}$ and $\gamma = \hbar/(2\tau_q)$, where τ_q is the quantum scattering time (see Supplementary Information and Ref. [28]).

The connection between the description given by $\Omega(\bar{\mu}, B)$ and $\Omega_{\text{disk}}(\mu, B)$ can be understood as though the external control parameter $\bar{\mu}$ determines, along with B , the control parameter of the graphene disk. More specifically, the magnetic field dependence of μ is a consequence of the finite value of the geometric capacitance C_{g} , since $\bar{\mu} = e^2n(B)/C_{\text{g}} + \mu$. If we ideally think of removing the moveable capacitor by directly applying the voltage to the graphene sheet, i.e. $C_{\text{g}} \rightarrow \infty$, the two control parameters coincide, implying that the dependence of μ on B , for finite C_{g} , can be interpreted as a feature of the measurement setup and not an intrinsic property of the material sample (graphene in our case). Similarly, the measurement of thermodynamic quantities associated with $\Omega_{\text{osc}}(\mu, B)$ (such as $\chi_{\text{m,osc}} = e^2\partial M_{\text{osc}}/\partial B$ and $C_{\text{q,osc}} = e^2\partial n_{\text{osc}}/\partial\mu$) represent a direct probe of the properties of the sample.

The general observation allowing to relate the frequency shift given in Eq. (2) to the dHvA effect, is that both the quantum capacitance $C_{\text{q,osc}} = e^2\partial n_{\text{osc}}/\partial\mu$ and the magnetic susceptibility oscillations $\chi_{\text{m,osc}} = e^2\partial M_{\text{osc}}/\partial B$ are a manifestation of the same underlying phenomenon, i.e. the Landau level structure of graphene, ultimately described by the thermodynamic potential $\Omega_{\text{disk}}(\mu, B)$. For the case of graphene, we can establish a relation between $C_{\text{q,osc}}$ and $\chi_{\text{m,osc}}$,

$$C_{\text{q,osc}} = \frac{\chi_{\text{m,osc}}}{\Gamma(\mu, B)}, \quad (4)$$

where, for $\mu \gg \gamma$, $\Gamma(\mu, B) = \left(\frac{\mu}{2eB}\right)^2$ (see Supplementary Information). Equation (4) directly translates the quantum capacitance oscillations with the magnetic field into oscillations of the magnetic susceptibility. While the analytical relation (4) is specific to graphene, it is possible to apply the same idea to other materials: the analytical structure of $\Omega_{\text{disk}}(\mu, B)$

implies that the origin of the oscillatory behavior of C_q and χ_m is shared and it is therefore possible to relate the two.

From Eq. (4), considering the case of negligible $\Delta\mu$ it is also possible to express the frequency shift given in Eq. (2) as a function of χ_m as

$$\Delta f_n = \left[\frac{\partial f_{0,n}}{\partial V} C_g V_g - \frac{f_{0,n}}{2k_{0,n}} (C'_g V_g)^2 \right] \frac{\chi_{m,osc}/\Gamma(\mu, B)}{C_{q,0} [C_{q,0} + \chi_{m,osc}/\Gamma(\mu, B)]}, \quad (5)$$

where $C_{q,0} = e^2 \partial n_0 / \partial \mu = N e^2 \mu / (\pi v_F^2 \hbar^2)$, with the spin degeneracy factor $N = 2$. The relation given in Eq. (5) allows us to infer the oscillations of the magnetic susceptibility, characteristic of the dHvA effect, directly from the frequency shift measurement in the graphene Corbino disk. Furthermore, Eq. (5) allows us to establish the optimal value of the gate voltage $V_g = \frac{C_g k_{0,n}}{C'_g f_{0,n}} \frac{\partial f_{0,n}}{\partial V}$ leading to the maximum frequency shift.

QUANTUM HALL STATES AND MECHANICAL RESONANCES

In our measurements, we observed frequency shifts Δf , consistent with Eqs. (2,5), in the Au resonator across the incompressible ranges of QH states. Fig. 3a displays the magnetic field dependence of frequency points at which the measured phase of the mixing current flips 180° . The separation of these phase flips marks the linewidth of the resonance; the data were obtained in device B2 at $V_g = \pm 30V$. The overlaid traces are calculated according to the theoretical model for the dHvA effect given by Eq. (5). The data indicate equivalent dHvA behavior for electrons and holes, which was also verified at other gate voltage values. The extracted quantum scattering time $\tau_q = \frac{\hbar}{\gamma}$ reduces as V_g increases, which is corroborated by a similar behavior in our other devices. We resolve Δf down to ~ 25 Hz, but for some magnetic field ranges, e.g. around $\nu = 2$ in Fig. 3b, the magnitude of the frequency shift is not observable due to the low conductivity at the incompressible QH states. Another low-conductivity regime in Fig. 3b is seen above 2.3 T, related to the state $\nu = 0$. In addition to the integer QH states, several fractional QH states are observed in these devices [30], bearing witness to the sensitivity of our detection scheme.

It is worth noting that the theory predictions shown in Fig. 3 are explicitly derived using the energy spectrum of massless Dirac electrons $\epsilon_n = \text{sign}(n) \hbar \omega_D \sqrt{|n|}$ implying a Berry phase $\gamma = \pm \pi$ [29]. Even though gold resonances are heavily utilized, we are probing the magnetization properties of the graphene part of the structure: Choosing the spectrum and

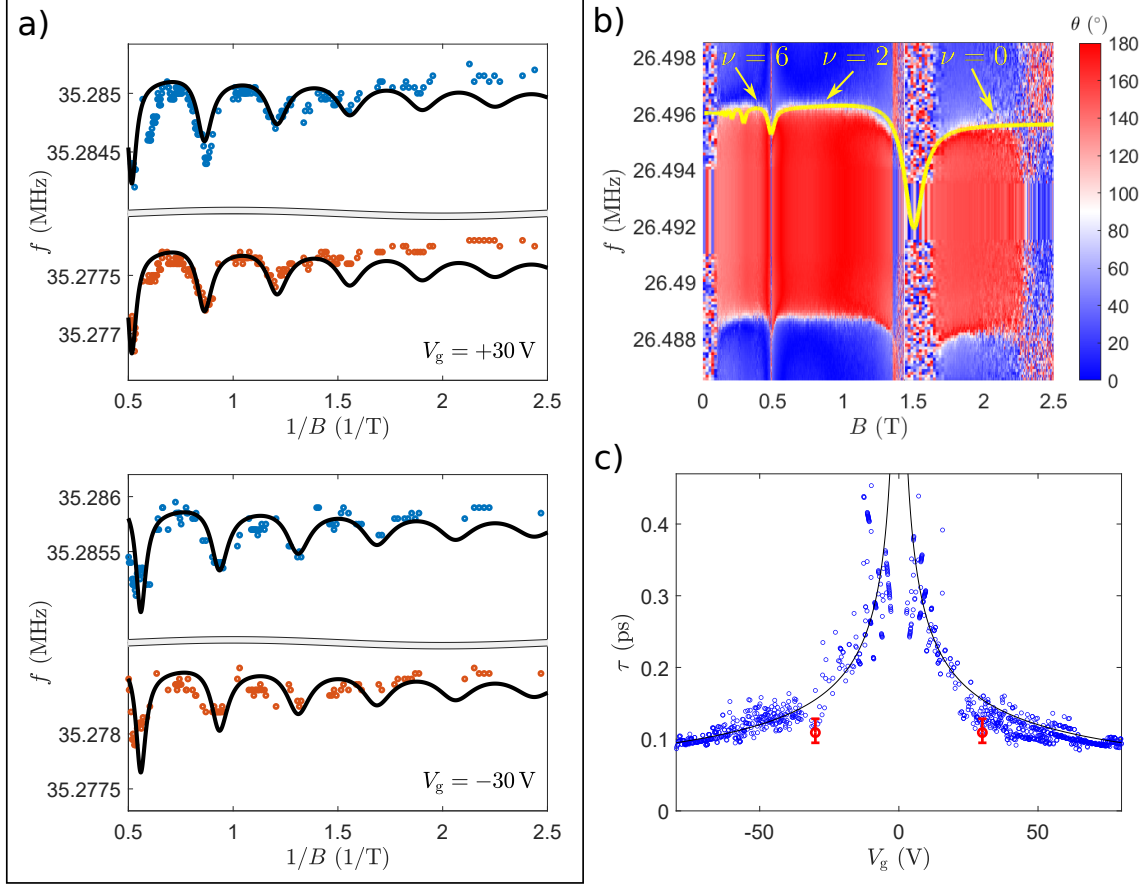


FIG. 3. **Mechanical resonance frequency shift due to de Haas – van Alphen effect.** a) Upper (blue dots) and lower (red dots) edges of the 35 MHz resonance in the B2 device at gate voltages $V_g = \pm 30$ V as a function of $1/B$. The edge points correspond to the frequencies where the phase of the mechanically induced mixing current flips by 180 degrees (see Fig. 2). The solid lines denote the theoretical fits with scattering times of $\tau_q \approx 0.11$ ps at $V_g = \pm 30$ V. b) Mixing current phase (θ) of the 26.5 MHz resonance in the device B1.5 presented as a function of B . The yellow line depicts the theoretical estimate with $\tau_q \approx 0.19$ ps scattering time. c) Quantum scattering time τ_q extracted from dHvA measurement in Fig. 3a (red markers), and the equivalent time τ_S from SdH oscillations in Fig. 2a (blue markers). The red error bars show a 15% deviation from the chosen Landau level widths γ in Fig. 3a that still reproduce a good agreement between the theory and the experiment. The solid black line denotes $\tau \propto 1/\sqrt{V_g}$ trend.

Berry phase of 2D electron gas would result in a different spacing of the frequency dips.

In Fig. 3b, we present the phase of the mixing current measured in the device B1.5 at the 26.5 MHz resonance at $V_g = 7$ V as a function of perpendicular magnetic field. The overlaid curve is calculated from Eqs. (2,5) in which two fitting parameters were employed: $\partial f_{0,n}/\partial V = 35$ kHz/V and the quantum scattering time $\tau_q = 0.19$ ps. Equally good agreement is obtained for the lower phase flip as the width of the middle region (line width of the resonance) is unchanged across the measured magnetic field range. The fit-value of the scattering time is close to $\tau_S = 0.3$ ps extracted from Shubnikov–de Haas oscillations at $V_g = 10$ V in a similar device previously [23], and also close to the data in Fig. 3c below. The general structure of the frequency modulation behavior $f(B)$ can be well understood by Eq. (2), according to which the frequency dips are produced by the $-\frac{\partial f_{0,n}}{\partial V} \left[C_g V_g \Delta \frac{1}{C_q} \right]$ term and the shift in the frequency level across the transition at $B = 1.5$ from $\nu = 2$ to $\nu = 0$ arises from the ensuing $\Delta\mu \simeq 30$ meV (see Fig. S3). The last term in Eq. (2), which would create positive peaks in the frequency shifts, is negligible with the parameters corresponding to our experiment.

In Fig. 3c, the scattering times τ_q obtained from the dHvA fits are plotted as a function of V_g along with the values τ_S obtained from the Shubnikov-de Haas oscillations, present in the Landau fan plot in Fig. 2a. At small charge density, our value for τ_S matches with the scattering time obtained in Ref. [31] for ultraclean suspended graphene. The correspondence between the experimentally determined values of τ_q and τ_S corroborates the interpretation that our measured frequency shifts in $f(B, V_g)$, indeed arise from the dHvA effect in graphene.

OUTLOOK

Compared to the other mechanical resonance measurements with graphene samples in magnetic fields [15, 16], our approach is different as we probe the graphene via a Au beam resonator. In a way our work is similar to the cantilever experiments by Harris and coworkers [11]: however, by using a “second cantilever”, the inner contact, we can facilitate operation on any conducting 2D material and obtain extraordinary sample quality via current annealing. This achievement seems out of reach for regular cantilever devices combined with the present state-of-the-art nanofabrication possibilities for 2D material. From this perspec-

tive, our setup opens up new possibilities in relation to the investigation of the magnetic properties of transition metal dichalcogenides (see e.g. [32–34]), with particular reference to the role of local symmetry breaking in the appearance of magnetic moments and hidden interactions in centrosymmetric crystals [35–37].

In conclusion, we have developed a versatile system of coupled resonators in which a Au resonator can be employed for sensing of forces originating in atomically thin suspended samples, made of graphene in the QH regime in our case. Owing to the free suspension of our graphene membrane, movement of the Au sensing element can be detected via displacement of the graphene, which facilitates force sensitivity sufficient to observe magnetization oscillations due to the de Haas–van Alphen effect in integer QH states, and even in the fractional QH regime. The experimental approach developed in this work opens up the possibility to investigate de Haas–van Alphen effect in other 2D materials, in particular transition metal dichalcogenide crystals with hidden magnetic properties.

We thank V. Falko, M. Kumar, and S. Paraoanu for useful discussions. This work was supported by the Academy of Finland projects 314448 (BOLOSE) and 336813 (CoE, Quantum Technology Finland) as well as by ERC (grant no. 670743). This research project utilized the Aalto University OtaNano/LTL infrastructure which is part of European Microkelvin Platform. A.L. is grateful to Osk. Huttunen foundation for scholarship. J.M. thanks the support of the Väisälä Foundation of the Finnish Academy of Science and Letters.

METHODS

Sample fabrication and measurement setting

Our Au resonators with suspended graphene Corbino disks were fabricated using a method adapted from Ref. [38] and described in depth in Ref. [23]. The fabrication was based on selective manipulation of the two different resists with electron beam: PMMA for defining metal contacts, and lift-off-resist (LOR) for support of suspended structures. The Cr/Au contacts were deposited using ultra-high vacuum metal evaporation in two steps with an LOR layer spun to separate the bottom contact defining the outer rim of the Corbino device, while the top contact supported by the separation layer bridged to the middle of the Corbino ring. The thickness of the Au electrodes amounted to $h_L = 70$ nm (the lower

electrode) and $h_U = 120$ nm (the upper electrode).

The whole structure was supported by $t_V = 500$ nm of LOR standing on a standard $t_{Si} = 300$ nm thick SiO_2 covered Si++ substrate that served as a back gate. Thus, the vacuum gap (thickness t_V) and SiO_2 as insulating layers yield $d_{\text{eff}} = t_V + t_{Si}/\epsilon_r = 580$ nm for the effective gap of the gate capacitor. This corresponds to the geometric gate capacitance value $C_g \approx 1.15 \times 10^{-5}$ F/m² obtained from the measured Landau fan diagram. Furthermore, the mechanical resonant frequencies at $B = 0$ exhibit the expected capacitive softening behavior. Due to the built-in strain and a rather large distance between the graphene and the gate electrodes, our graphene membranes easily sustain voltages up to $V_g = 100$ V.

The fabricated sample chips were glued into sample boxes with microwave striplines that in turn could be wire bonded to the bonding pads of the Corbino devices. The sample boxes were connected to the measurement lines through bias tees that allowed the DC conductance measurements and low frequency readout of the mechanical resonance, as well as the high frequency RF input used to transduce the mechanical motion.

The results presented here were obtained on two samples, B1.5 and B2, in which the Au beams were connected graphene Corbino disks with outer (inner) diameter of 3.8 (1.5) and 4.5 (1.8) μm , respectively. The length of the main, lower Au resonator, connected to the outer rim of graphene, was approximately 8 μm , with a cross section of 70 nm \times 5 μm . The best results were obtained using resonance frequencies around 25 – 35 MHz, which corresponds to the third harmonic our 8- μm -long Au beam. Quality factors of these resonances amounted to ~ 4000 .

The fabricated devices were characterized using standard conductance measurement techniques and resonance measurements at 10 mK. The devices were mounted slightly off center of the 9 T magnet on a Bluefors LD400 dilution refrigerator. At the sample location, $dB/dz = 60$ T/m and $d^2B/dz^2 = 1100$ T/m² with a maximum field of 6.8 T. This second derivative has such a tiny effect on the Au mechanical frequencies so that it can be neglected in our force analysis.

Prior to the actual measurements, however, current annealing [39] was performed by applying a bias voltage $V_b \approx 2$ V across the Corbino ring, consequently evaporating residues from fabrication off from the graphene flake. The device quality was assessed by measuring the Landau fan diagram, such diagram is presented in Fig. 2a for the investigated sample

B2. Note the fractional QH state $\nu = 1/3$ is visible from $B \approx 3$ T upwards along with the usual set of integer quantum Hall states highlighting the good quality of the measured samples. At higher fields more fractional states appeared, see Refs. [22, 23].

Identification of quantum Hall states

Detection of the QH states in the graphene Corbino was performed both using low-frequency AC conductance and the mechanical response of the combined gold-graphene modes. The sensitive Au resonance detection of QH states via graphene's mechanical response is facilitated by the variation of the derivative dG/dV_g that specifies the magnitude of the mixing current I_{mix} in graphene (see Eq. (6)). Consequently, I_{mix} pinpoints regions with $dG/dV_g = 0$, across which the mixing current changes its sign. In the experiment, the sign change of I_{mix} is seen as a flip of the phase by π in the down-mixed signal. Fig. 2c displays the measured conductance $G(V_g)$ and the phase of the mixing current. An exact match between $dG/dV_g = 0$ locations (traditional location of the QH state) and the phase flips is observed.

Mechanical resonances

Mechanical resonances were detected using the FM mixing technique [24]. In this technique an FM-modulated signal $V^{\text{FM}}(t) = V^{\text{AC}} \cos(2\pi f_c t + (f_\Delta/f_L) \sin(2\pi f_L t))$ was fed to the center electrode of the Corbino device through a bias tee. Here V^{AC} and f_c are the carrier amplitude and frequency, respectively. The sinusoidal low-frequency modulation signal at f_L (typically ~ 600 Hz) was supplied by the SR830 lockin amplifier, while the frequency deviation f_Δ (typically 1-4 kHz) was produced by the frequency generator (Rohde & Schwarz SMY01, or Keysight N9310A) producing the FM-modulated signal.

The FM-modulated signal, applied across source-drain electrodes of the graphene membrane, got downmixed by the intrinsic nonlinearity of the graphene device, and the low frequency component at the frequency f_L reflects the mechanical motion amplitude z of the graphene flake. This proportionality can be expressed as

$$I_{\text{mix}} \propto \frac{C'_{\text{tot}}}{C_{\text{tot}}} \frac{\partial G}{\partial V_g} \left| \frac{\partial \text{Re}(z)}{\partial f} \right|, \quad (6)$$

where $C_{\text{tot}} = (1/C_g + 1/C_q)^{-1}$ is the total capacitance, and $C'_{\text{tot}} = \frac{dC_{\text{tot}}}{dz}$. C_g and C_q are the gate capacitance and the quantum capacitance per unit area, respectively. Phase shifts may occur between the drive and the response due interference phenomena in the flexural waves traveling along the Corbino disk, driven from the outer edge. In the case of phase shifts, the mechanical response function $\frac{\partial \text{Re}(z)}{\partial f}$ will obtain a corresponding reference phase, which results in a combination of dispersive and absorptive parts of the mechanical response.

The observed combined gold-graphene modes below ~ 40 MHz involve either the lower or upper Au electrode beam, the motion of which is followed by graphene at master-slave principle owing to the time-dependent boundary conditions imposed by Au on graphene. The 35.3 MHz resonance of the B2 device depicted in Fig. 2d, for example, is detected with the measurement configuration shown in Fig. 1 but is not observable when the source and drain sides are reversed implying that this mechanical mode is dominated by the movement of the lower gold beam with the graphene sheet following. Moreover, it is this exclusive reliance on the mechanical Au resonances in actuation and detection, regardless of the properties of graphene, that allows us to generalize our investigation method to other 2D materials.

In our frequency sweeps of the sample B1.5, we observed 12 mechanical modes below 27 MHz. Using COMSOL simulations, candidate mode shapes for these modes could be identified. We utilized simulated gate voltage dependencies for each mode to determine the mode shape corresponding to the 26.5 MHz resonance with which the dHvA effect was observed. A mode shape, where the most significant role is played by the cantilever, displays a weak frequency increase with respect to the gate voltage in the simulations corresponding to the observed trend in the measurements.

We emphasize that our detection scheme for magnetization effects in a 2D material relies on finding well-defined resonances of the gold structure and is, therefore, suitable for a very wide variety 2D systems. Specifically, the 2D-material portion of the structure is not required to have good resonator properties. For example, in our case, the resonances shown here have quality factors of the order of 1000.

In addition to graphene and Au modes, surface waves around 20 MHz were excited in the LOR-layer by the microwave drive [40]. Even though these modes could be excited at very small power, they were not useful for detection purposes owing to the small $Q = 100 - 200$.

The sensitivity of our experiments is set by the frequency resolution of the resonance peak position, approximately 25 Hz. This frequency resolution corresponds to $\sim 10^4$ Bohr

magneton, which is six orders of magnitude better than in the torque magnetometer work of Ref. [7]. Compared with the cantilever work of Ref. [10], our sensitivity is two orders of magnitude better. After optimization of the device parameters and improving the frequency resolution, similar sensitivity as in the work of Bleszynski-Jayich et al. can be obtained [11].

Fitting the theory predictions

The theoretical predictions of the frequency shift due to the dHvA effect given in Eq. (2) are fitted to the experimental data as shown in Figs. 3a and 3b. To obtain the spring constant of the modes, we assume that the effective mass of the modes is determined by the gold resonator, and graphene's contribution is practically negligible. We approximate that, for the B2 device ~ 80 nm thick lower gold beam, the 2D density is $\rho \approx 1.5 \times 10^{-3}$ kg/m², and $\rho \approx 2.1 \times 10^{-3}$ kg/m² for the ~ 110 nm thick cantilever of B1.5.

For our setup, the last term of the frequency shift in Eq. (2) is negligible and, therefore, the size of the frequency shift is scaled by the factor $\partial f_{0,n}/\partial V$. We fit $\partial f_{0,n}/\partial V$ to the experimental data to obtain proper magnitude of Δf together with the Landau level width γ that affects the magnitude of Δf as well as the width of the frequency dips. For the device B2 (B1.5) we have 16 kHz/V (35 kHz/V). The larger value for the B1.5 device mode is expected due to it being a mode of the cantilever whose other end is attached to the graphene. This boundary condition makes the B1.5 mode more sensitive to tensioning effects than the resonance of the lower gold plate of the B2 device.

The scattering time $\tau_S = \hbar\sqrt{\pi n}\mu_q/ev_F$ shown in Fig. 3c was calculated from the quantum mobility μ_q , which in turn was obtained by extracting the minimum field of Shubnikov–de Haas oscillations $B_0(V_g)$ and using the relation $\mu_q B_0 = 1$. Additionally, the error bars of τ_q in the same figure show a 15% deviation from the values of $\gamma = \hbar/(2\tau_q)$ used to fit the theory curves in Fig. 3a. Values of γ within this tolerance reproduce a good agreement of Δf between the theory and the experiment.

Supplementary Information

Details of the theoretical results.

* These two authors contributed equally

† pertti.hakonen@aalto.fi

- [1] L. Landau, *Zeitschrift für Physik* **64**, 629 (1930).
- [2] R. Peierls, *Zeitschrift für Physik* **80**, 763 (1933).
- [3] Z. F. Ezawa, *Quantum Hall Effects* (WORLD SCIENTIFIC, 2013), 3rd ed.
- [4] V. T. Dolgoplov, *Physics - Uspekhi* **57**, 105 (2014).
- [5] I. A. Luk'yanchuk, *Low Temperature Physics* **37**, 45 (2011).
- [6] J. P. Eisenstein, H. L. Stormer, V. Narayanamurti, A. Y. Cho, A. C. Gossard, and C. W. Tu, *Phys. Rev. Lett.* **55**, 875 (1985).
- [7] S. A. Wieggers, M. Specht, L. P. Lévy, M. Y. Simmons, D. A. Ritchie, A. Cavanna, B. Etienne, G. Martinez, and P. Wyder, *Physical Review Letters* **79**, 3238 (1997).
- [8] A. Wixforth, J. Sciba, M. Wassermeier, J. P. Kotthaus, G. Weimann, and W. Schlapp, *Phys. Rev. B* **40**, 7874 (1989).
- [9] H. Okamoto, W. Izumida, Y. Hirayama, H. Yamaguchi, A. Riedel, and K.-J. Friedland, *Phys. Rev. B* **89**, 245304 (2014).
- [10] J. G. E. Harris, D. D. Awschalom, F. Matsukura, H. Ohno, K. D. Maranowski, and A. C. Gossard, *Applied Physics Letters* **75**, 1140 (1999).
- [11] A. C. Bleszynski-Jayich, W. E. Shanks, B. Peaudecerf, E. Ginossar, F. von Oppen, L. Glazman, and J. G. E. Harris, *Science (New York, N.Y.)* **326**, 272 (2009).
- [12] K. S. Novoselov, A. K. Geim, S. V. Morozov, D. Jiang, M. I. Katsnelson, I. V. Grigorieva, S. V. Dubonos, and A. A. Firsov, *Nature* **438**, 197 (2005).
- [13] Y. Zhang, Y. W. Tan, H. L. Stormer, and P. Kim, *Nature* **438**, 201 (2005).
- [14] Z. Tan, C. Tan, L. Ma, G. T. Liu, L. Lu, and C. L. Yang, *Physical Review B - Condensed Matter and Materials Physics* **84**, 2 (2011).
- [15] V. Singh, B. Irfan, G. Subramanian, H. S. Solanki, S. Sengupta, S. Dubey, A. Kumar, S. Ramakrishnan, and M. M. Deshmukh, *Appl. Phys. Lett.* **100**, 233103 (2012).
- [16] C. Chen, V. V. Deshpande, M. Koshino, S. Lee, A. Gondarenko, A. H. MacDonald, P. Kim, and J. Hone, *Nature Phys.* **12**, 240 (2016).

- [17] M. C. Lemme, S. Wagner, K. Lee, X. Fan, G. J. Verbiest, S. Wittmann, S. Lukas, R. J. Dolleman, F. Niklaus, H. S. J. van der Zant, et al., *Research* **2020**, 8748602 (2020).
- [18] M. Šiškins, M. Lee, S. Mañas-Valero, E. Coronado, Y. M. Blanter, H. S. J. van der Zant, and P. G. Steeneken, *Nature Communications* **11**, 2698 (2020).
- [19] P. G. Steeneken, R. J. Dolleman, D. Davidovikj, F. Alijani, and H. S. J. van der Zant, *2D Materials* **8**, 042001 (2021).
- [20] M. Kamada, A. Laitinen, W. Zeng, M. Will, J. Sarkar, K. Tappura, H. Seppä, and P. Hakonen, *Nano Letters* **21**, 7637 (2021).
- [21] X. Song, M. Oksanen, M. A. Sillanpää, H. G. Craighead, J. M. Parpia, and P. J. Hakonen, *Nano letters* **12**, 198 (2012).
- [22] A. Laitinen, M. Kumar, and P. J. Hakonen, *Phys. Rev. B* **97**, 075113 (2018).
- [23] M. Kumar, A. Laitinen, and P. Hakonen, *Nature Communications* **9** (2018).
- [24] V. Gouttenoire, T. Barois, S. Perisanu, J. L. Leclercq, S. T. Purcell, P. Vincent, and A. Ayari, *Small* **6**, 1060 (2010).
- [25] A. Eichler, J. Moser, J. Chaste, M. Zdrojek, I. Wilson-Rae, and A. Bachtold, *Nature Nanotech.* **6**, 339 (2011).
- [26] L. A. Ponomarenko, R. Yang, R. V. Gorbachev, P. Blake, A. S. Mayorov, K. S. Novoselov, M. I. Katsnelson, and A. K. Geim, *Phys. Rev. Lett.* **105**, 136801 (2010).
- [27] G. L. Yu, R. Jalil, B. Belle, A. S. Mayorov, P. Blake, F. Schedin, S. V. Morozov, L. A. Ponomarenko, F. Chiappini, S. Wiedmann, et al., *PNAS* **110**, 3282 (2013).
- [28] S. G. Sharapov, V. P. Gusynin, and H. Beck, *Phys. Rev. B* **69**, 075104 (2004).
- [29] M. I. Katsnelson, *Graphene: Carbon in Two Dimensions* (Cambridge University Press, 2012).
- [30] A. Laitinen, J. Manninen, F. Massel, and P. Hakonen, To be submitted (2021).
- [31] K. Bolotin, K. Sikes, Z. Jiang, M. Klima, G. Fudenberg, J. Hone, P. Kim, and H. Stormer, *Solid State Communications* **146**, 351 (2008).
- [32] Z. Wang, J. Shan, and K. F. Mak, *Nature Nanotechnology* **12**, 144 (2017).
- [33] R. Pisoni, A. Kormányos, M. Brooks, Z. Lei, P. Back, M. Eich, H. Overweg, Y. Lee, P. Rickhaus, K. Watanabe, et al., *Physical Review Letters* **121**, 247701 (2018).
- [34] S. Manzeli, D. Dumcenco, G. Migliato Marega, and A. Kis, *Nature Communications* **10**, 1 (2019).
- [35] X. Zhang, Q. Liu, J.-W. Luo, A. J. Freeman, and A. Zunger, *Nature Physics* **10**, 387 (2014).

- [36] L. Yuan, Q. Liu, X. Zhang, J. W. Luo, S. S. Li, and A. Zunger, *Nature Communications* **10** (2019).
- [37] L. Du, T. Hasan, A. Castellanos-Gomez, G. B. Liu, Y. Yao, C. N. Lau, and Z. Sun, *Nature Reviews Physics* **3**, 193 (2021).
- [38] N. Tombros, A. Veligura, J. J. Junesch, J. van den Berg, P. J. Zomer, M. Wojtaszek, I. J. Vera Marun, H. T. Jonkman, and B. J. van Wees, *J. Appl. Phys.* **109**, 093702 (2011).
- [39] J. Moser, A. Barreiro, and A. Bachtold, *Applied Physics Letters* **91**, 163513 (2007).
- [40] A. Laitinen, J.-P. Kaikkonen, T. S. Abhilash, I. Todoshchenko, J. Manninen, V. Zavyalov, A. Savin, A. Isacsson, and P. J. Hakonen, *Journal of Physics D: Applied Physics* **52**, 24LT02 (2019).

De Haas–van Alphen effect in graphene – Supplementary material

Juuso Manninen,^{1,2,*} Antti Laitinen,^{1,3,*} Francesco Massel,^{4,5,†} and Pertti Hakonen^{1,2}

¹*Low Temperature Laboratory, Department of Applied Physics,
Aalto University School of Science, P.O. Box 15100, 00076 Aalto, Finland*

²*QTF Centre of Excellence, Department of Applied Physics,
Aalto University, PO Box 15100, FI-00076 AALTO, Finland*

³*Department of Physics, Harvard University, Cambridge, MA 02138, USA*

⁴*Department of Physics, Nanoscience Center, University of Jyväskylä, FIN 40014, Finland*

⁵*Department of Science and Industry Systems, University of South-Eastern Norway, PO Box 235, Kongsberg, Norway*

THERMODYNAMIC ANALYSIS AND FORCES ACTING ON A MOVABLE CAPACITOR (FINITE C_q)

Let us consider the energy per unit area of a capacitor with one of the plates constituted by a finite-DOS material (in our case graphene), in the presence of an external magnetic field B

$$U(n, B) = \frac{1}{2} \frac{e^2 n^2}{C_g} + \Xi(n, B). \quad (\text{S1})$$

The first term in Eq. (S1) is the energy associated with the electrical field building up between the plates of the capacitor, whereas the second corresponds to the energy related to the finite density of states (DOS) of the system. In this description, the charge n on the capacitor plates and the magnetic field B are the control parameters.

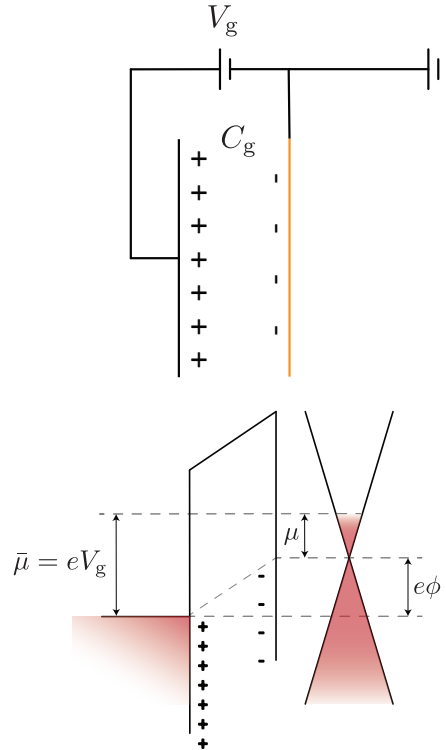


FIG. S1. Top. Lumped-elements description of a capacitor with one plate constituted by a finite-DOS material (yellow) to which a voltage V_g is applied. Bottom. The voltage drop leads to the buildup of an electric field between the capacitor plates, corresponding to an electrostatic potential drop ϕ . Owing to the finite DOS, part of the energy provided by the voltage source goes into promoting electrons to higher-energy single-particle states (increase of the chemical potential μ).

Considering a standard thermodynamic relation [1], we can define the electrochemical potential as

$$\bar{\mu} = \left(\frac{\partial U}{\partial n} \right)_{z,B} = \frac{e^2 n}{C_g} + \mu(n) \quad (\text{S2})$$

implying $n = \frac{C_g}{e^2} (\bar{\mu} - \mu)$. This relation, written as

$$\frac{\bar{\mu}}{e} = \frac{en}{C_g} + \frac{\mu}{e},$$

allows us to show that, for $C_g \rightarrow \infty$, the tunability of the electrochemical potential $\bar{\mu}$ is directly translated into the tunability of the chemical potential of the membrane μ . Here $\bar{\mu}$ is the electrochemical potential consisting of the electrostatic $e\phi = \frac{e^2 n}{C_g}$ and chemical $\mu = \frac{\partial \Xi}{\partial n}$ potentials [2].

We can now consider the thermodynamic potential $\Omega(\bar{\mu})$ where $\bar{\mu}$ (not μ nor ϕ) is the independent control parameter, along with B . From equation (S1), we obtain

$$\Omega(\bar{\mu}, B) = U(n, B) - \bar{\mu}n = \frac{1}{2} \frac{C_g}{e^2} (\bar{\mu} - \mu)^2 + \Phi(\bar{\mu}, z) - \bar{\mu}n, \quad (\text{S3})$$

where we have defined $\Phi(\bar{\mu}, B) \doteq \Xi(n(\bar{\mu}, B))$. Using equation (S3), we can calculate the force for constant $\bar{\mu}$, i.e. at constant external applied voltage

$$V_g \doteq \frac{\bar{\mu}}{e} = \frac{en}{C_g} + \frac{\mu}{e}. \quad (\text{S4})$$

To this end, let us obtain a preliminary result

$$\begin{aligned} \frac{\partial n}{\partial z} &= C'_g e \left(V_g - \frac{\mu}{e} \right) - \frac{C_g}{e^2} \frac{\partial \mu}{\partial n} \frac{\partial n}{\partial z} = \frac{C'_g}{e} \left(V_g - \frac{\mu}{e} \right) - \frac{C_g}{C_q} \frac{\partial n}{\partial z} \\ \Rightarrow \frac{\partial n}{\partial z} &= \left(1 + \frac{C_g}{C_q} \right)^{-1} \frac{C'_g}{e} \left(V_g - \frac{\mu}{e} \right), \end{aligned} \quad (\text{S5})$$

where $C_g = \partial C_g / \partial z$. Equation (S5) implies, in addition, that

$$\frac{\partial \mu}{\partial z} = \frac{C'_g}{(C_q + C_g)} (eV_g - \mu) \quad (\text{S6})$$

and that the electrostatic force per unit area can be expressed as

$$\begin{aligned} F &= -\frac{\partial \Omega}{\partial z} = -\frac{1}{2} C'_g \left(V_g - \frac{\mu}{e} \right)^2 + \frac{C_g}{e} \left(V_g - \frac{\mu}{e} \right) \frac{\partial \mu}{\partial n} \frac{\partial n}{\partial z} - \mu \frac{\partial n}{\partial z} + eV_g \frac{\partial n}{\partial z} \\ &= -\frac{1}{2} C'_g \left(V_g - \frac{\mu}{e} \right)^2 + \frac{C_g}{C_q} e \left(V_g - \frac{\mu}{e} \right) \frac{\partial n}{\partial z} + e \left(V_g - \frac{\mu}{e} \right) \frac{\partial n}{\partial z} \\ &= -\frac{1}{2} C'_g \left(V_g - \frac{\mu}{e} \right)^2 \left(1 - 2 \frac{1 + \frac{C_g}{C_q}}{1 + \frac{C_g}{C_q}} \right) \\ &= \frac{1}{2} C'_g \left(V_g - \frac{\mu}{e} \right)^2, \end{aligned} \quad (\text{S7})$$

which is consistent with the expression given in the literature about carbon nanotubes [3, 4].

As discussed in the main text, the distinguishing factor between the full thermodynamic potential $\Omega(\bar{\mu}, B)$ and that of the graphene disk $\Omega_{\text{disk}}(\mu, B)$ is the control parameter $\bar{\mu}$ versus μ . In Fig. S2, we have compared the behavior of the oscillatory components of magnetization M_{osc} and magnetic susceptibility $\chi_{\text{m,osc}}$, see the derivations below, as a function of B^{-1} with $\bar{\mu}$ and μ as a control parameter.

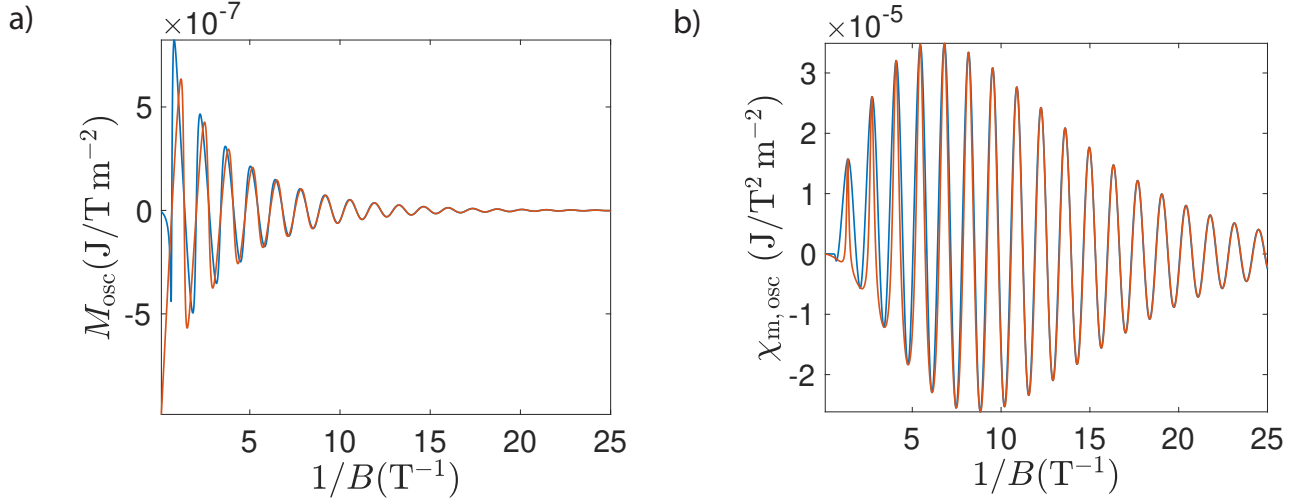


FIG. S2. a) Magnetization oscillations obtained from equation S3 using $v_F = 10^6 \text{ m/s}$ and $\tau_q = 0.19 \text{ ps}$ at fixed $\mu = 31 \text{ meV}$ (red) and $\mu(B)$ for $C_g \approx 1.15 \times 10^{-5} \text{ F/m}^2$ (blue), where the Lorentzian broadening with the same disorder has been taken into account. b) The oscillating part $\chi_{m,\text{osc}}$ of magnetic susceptibility $\chi_m(\mu, B)$ for the same parameters as in panel a).

FREQUENCY SHIFT

Given the expression for the force of Eq. (S7) (Eq. (1) of the main text), we evaluate here the mechanical frequency shift for a mechanical resonator whose electrical properties can be described by Eq. (S1).

For sake of simplicity, we focus here on the analysis of a membrane (vanishing flexural rigidity) in the presence of uniform tension. The only difference with the general case (finite flexural rigidity and nonuniform tension) is the specific value of the mechanical frequency in absence of external applied voltage $\omega_{0,n}$, which is not central to our argument.

Firstly, we notice that the distance between the plates of the capacitor –and, consequently, the capacitance C_g – is modified by the application of the external electrostatic potential V_g (see Fig. S1). The equilibrium position of the movable capacitance $\xi_e = \xi_e(V_g, B)$ can be obtained from the solution of the general elastic equation for the structure (see e.g. [5] for the case of a graphene-only membrane).

The shifts of the mechanical resonant frequency $\omega_{0,n}$ for $V_g \neq 0$ can be determined considering the membrane position fluctuations around ξ_e . For a membrane, these fluctuations obey the following equation

$$\rho \ddot{\zeta} - T \Delta \zeta = \delta f(\mathbf{r}, t), \quad (\text{S8})$$

where we have defined $\delta f = [f(\xi_e + \zeta) - f(\xi_e)]$ and $T = T(\xi_e)$. The functions $\zeta(\mathbf{r}, t)$ and $\delta f(\mathbf{r}, t)$ in Eq. (S8) can be expanded as

$$\begin{aligned} \zeta(\mathbf{r}, t) &= \sum_{\mathbf{n}} \zeta_{\mathbf{n}} \exp[-i\omega_{\mathbf{n}} t] A_{\mathbf{n}}(\mathbf{r}), \\ \delta F(\mathbf{r}, t) &= \sum_{\mathbf{n}} \delta F_{\mathbf{n}} \exp[-i\omega_{\mathbf{n}} t] A_{\mathbf{n}}(\mathbf{r}), \end{aligned}$$

where $A(\mathbf{r})$ are the normal modes associated to the boundary value problem considered. Furthermore, approximating

$$\delta F_{\mathbf{n}} \simeq \left. \frac{\partial F}{\partial \zeta} \right|_{\xi_e} \zeta_{\mathbf{n}},$$

we obtain

$$\rho \omega_{\mathbf{n}}^2 \zeta_{\mathbf{n}} - T \lambda_{\mathbf{n}}^2 \zeta_{\mathbf{n}} = \left. \frac{\partial F}{\partial \zeta} \right|_{\xi_e} \zeta_{\mathbf{n}}, \quad (\text{S9})$$

leading to the following expression for the frequency of a given mode n

$$\omega_n = \sqrt{\omega_{0,n}^2 - \frac{1}{\rho} \left. \frac{\partial F}{\partial \zeta} \right|_{\xi_e}} \quad (\text{S10})$$

with $\omega_{0,n} = \sqrt{T\lambda_n^2/\rho}$, where λ_n depends on the geometry considered. For the case of a disk of radius R , we have that $\lambda_n \rightarrow \lambda_{i,j} = \alpha_{i,j}/R$, where $\alpha_{i,j}$ are the roots of the Bessel function $J_{i,j}(r)$. For the case of metallic leads (infinite DOS), we have that $\partial F/\partial \zeta = 1/2C_g''V_g^2$ allowing us to obtain from Eq. (S10) the usual capacitive softening voltage dependence of the mechanical resonant frequency.

In the case of finite DOS, from Eq. (S7), we can write

$$\left. \frac{\partial F}{\partial \zeta} \right|_{\xi_e} = \frac{1}{2}C_g'' \left(V_g - \frac{\mu}{e} \right)^2 - C_g' \left(V_g - \frac{\mu}{e} \right) \frac{1}{e} \left. \frac{\partial \mu}{\partial \zeta} \right|_{\xi_e}, \quad (\text{S11})$$

which with the help of Eq. (S6), gives

$$\left. \frac{\partial F}{\partial \zeta} \right|_{\xi_e} = \left\{ \frac{1}{2}C_g'' - \frac{C_g'^2}{C_q + C_g} \right\} \left(V_g - \frac{\mu}{e} \right)^2 \Big|_{\xi_e}. \quad (\text{S12})$$

Denoting by $\Delta\omega_n$ the difference between the resonant frequency at finite B with respect to the frequency at $B = 0$, we can write

$$\Delta\omega_n \simeq \Delta\omega_{0,n} - \frac{1}{2\rho\omega_{0,n}} \left(\left. \frac{\partial F}{\partial \zeta} \right|_B - \left. \frac{\partial F}{\partial \zeta} \right|_{B=0} \right), \quad (\text{S13})$$

where $\Delta\omega_{0,n} = \omega_{0,n}(B) - \omega_{0,n}(B = 0)$. The first term in Eq. (S13) represents the change of the resonant frequency with the external magnetic field associated with tensioning effects, whereas the second term is related to the magnetic field change of the capacitive softening term.

Noting that, for $B = 0$, the resonant frequency $\omega_{0,n}$ depends on the externally applied voltage only, we can approximate

$$\Delta\omega_{0,n} = \left. \frac{\partial\omega_{0,n}}{\partial V} \frac{\partial V}{\partial F} \right|_{B=0} \Delta F \simeq - \left. \frac{\partial\omega_{0,n}}{\partial V} \right|_{B=0} \frac{\Delta\mu}{e}. \quad (\text{S14})$$

Integrating equation (S6), in the limit $V_g \gg \mu/e$ and $C_q \gg C_g$, we have

$$\mu(B, \xi) = \mu(B) + \frac{eC_g(\xi)V_g}{C_q(B)}, \quad (\text{S15})$$

where the first term corresponds to the change in chemical potential as a function of B in the absence of capacitive detection ($C_g = 0$).

Equations (S14, S15) lead to

$$\Delta\omega_{0,n} = - \frac{\partial\omega_{0,n}}{\partial V} \left[\Delta\mu + C_g V_g \Delta \left(\frac{1}{C_q} \right) \right]. \quad (\text{S16})$$

Analogously, we have that

$$\left. \frac{\partial F}{\partial \zeta} \right|_B - \left. \frac{\partial F}{\partial \zeta} \right|_{B=0} \simeq -C_g'' V_g \left[\frac{\Delta\mu}{e} + C_g V_g \Delta \left(\frac{1}{C_q} \right) \right] - (C_g' V_g)^2 \Delta \left(\frac{1}{C_q} \right), \quad (\text{S17})$$

leading to

$$\Delta\omega_n = \left[- \frac{\partial\omega_{0,n}}{\partial V} + \frac{C_g'' V_g}{2\rho\omega_{0,n}} \right] \left[\frac{\Delta\mu}{e} + C_g V_g \Delta \frac{1}{C_q} \right] + \frac{(C_g' V_g)^2}{2\rho\omega_{0,n}} \Delta \left(\frac{1}{C_q} \right), \quad (\text{S18})$$

which with $\kappa_n = \rho\omega_n^2$ and $\omega_n = 2\pi f_n$ leads to Eq. (2) of the main text. We note also that, in the limit $C_g'' = 0$, Eq. (S18) corresponds to the expression given in [6] for the mechanical frequency shift.

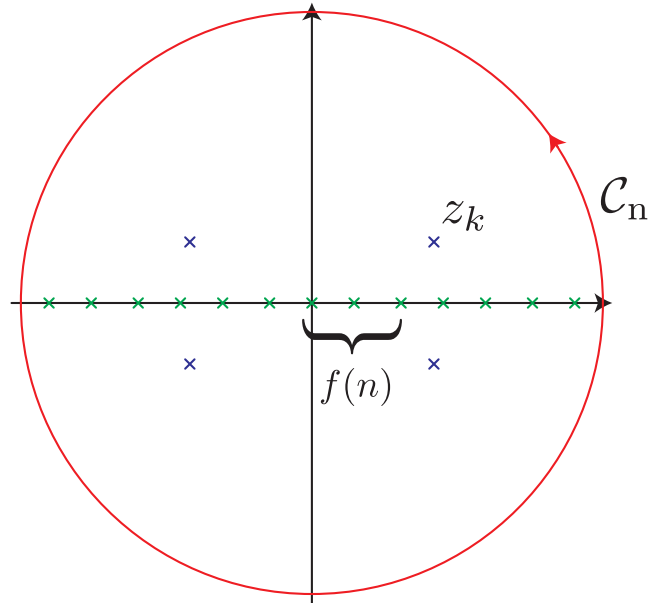


FIG. S3. Complex-plane representation of the relation in Eq. (S22). The red line represents the contour along which the integral on the lhs is performed. We have denoted the poles of $2\pi z \cot(\pi z)$ (whose residue is $f(n)$) in blue, whereas the poles of $f(z^2)$ are marked in red.

QUANTUM CAPACITANCE

We derive here the expression for the quantum capacitance C_q . To this end, we express the density of states as a sum of Lorentzians centered at $\epsilon_n = \text{sign}(n)\hbar\omega_D\sqrt{|n|}$ ($\omega_D = v_f\sqrt{2eB/\hbar}$)

$$D(\epsilon) = \frac{NeB}{2\pi\hbar} \sum_{n=-\infty}^{\infty} \frac{\gamma}{2\pi} \frac{1}{(\epsilon - \epsilon_n)^2 + \frac{\gamma^2}{4}} \quad (\text{S19})$$

with the spin degeneracy factor $N = 2$. Our analysis is based on the possibility of turning an infinite sum into an integral over the complex plane. If $f(w)$ is a meromorphic function, the following condition is fulfilled

$$\sum f(n) = \oint_{C_n} \pi \cot(\pi w) f(w) dw - \sum_k \text{Res} [\pi \cot(\pi w) f(w); w_k]. \quad (\text{S20})$$

Since, in our case, we have

$$f(n) = \frac{NeB}{2\pi\hbar} \frac{\gamma}{2\pi} \frac{1}{\left(\omega - \text{sign}(n)\omega_D\sqrt{|n|}\right)^2 + \frac{\gamma^2}{4}} \quad (\text{S21})$$

we operate a change of variables $w \rightarrow z^2$, which allows us to rewrite Eq. (S20) as

$$\sum f(n) = \oint_{C_n} 2\pi z \cot(\pi z) f(z^2) dz - \sum_k \text{Res} [2\pi z \cot(\pi z) f(z^2); z_k^2], \quad (\text{S22})$$

see Fig. S3 for the complex-plane representation of contours and poles leading to Eq. (S22).

The integral on the lhs of Eq. (S22) represents a (diverging) constant contribution, which can be renormalized by introducing an explicit frequency cutoff, analogously to what is done in Ref. [7]. Conversely, the second term, the sum over the poles of $2\pi z \cot(\pi z) f(z)$, can be evaluated explicitly, leading to the following expression for the density

of states

$$D(\epsilon) = \Lambda_D + \frac{N}{\pi v_F^2 \hbar^2} \frac{\epsilon \sinh \left[\frac{2\pi\gamma\epsilon}{(\hbar\omega_D)^2} \right] - \frac{\gamma}{2} \sin \left[\frac{2\pi(\epsilon^2 - \frac{\gamma^2}{4})}{(\hbar\omega_D)^2} \right]}{\cosh \left[\frac{2\pi\gamma\epsilon}{(\hbar\omega_D)^2} \right] - \cos \left[\frac{2\pi(\epsilon^2 - \frac{\gamma^2}{4})}{(\hbar\omega_D)^2} \right]}, \quad (\text{S23})$$

where Λ_D is the contribution coming from the integral on the contour C_n .

In the $\omega \gg \gamma$, ω_D limit the expression for $D(\omega)$ given in Eq. (S23), coincides with the one given in Ref. [7], in the same limit. From Eq. (S23) we can easily derive the expression for $C_q = e^2 D(\mu)$.

QUANTUM CAPACITANCE AND DE HAAS – VAN ALPHEN EFFECT

With an analogous calculation to the one leading to the expression for C_q , it is possible to derive an expression for the charge density n

$$n = n_0 + n_{\text{osc}} \quad (\text{S24})$$

with

$$n_0 = \frac{N}{2\pi v_F^2 \hbar^2} \left(\mu^2 - \frac{\gamma^2}{4} \right) \quad (\text{S25a})$$

$$n_{\text{osc}} = \frac{NeB}{\pi^2 \hbar} \arctan \left\{ \frac{\sin \left[\frac{2\pi}{(\hbar\omega_D)^2} \left(\mu^2 - \frac{\gamma^2}{4} \right) \right]}{\exp \left[\frac{2\pi\gamma\mu}{(\hbar\omega_D)^2} \right] - \cos \left[\frac{2\pi}{(\hbar\omega_D)^2} \left(\mu^2 - \frac{\gamma^2}{4} \right) \right]} \right\} \quad (\text{S25b})$$

and to the oscillatory component of the magnetization $M_{\text{osc}} = -\frac{\partial \Omega_{\text{osc}}}{\partial B}$

$$M_{\text{osc}} = -\frac{Ne}{2\pi^2 \hbar} \mu \arctan \left\{ \frac{\sin \left[\frac{2\pi}{(\hbar\omega_D)^2} \left(\mu^2 - \frac{\gamma^2}{4} \right) \right]}{\exp \left[\frac{2\pi\gamma\mu}{(\hbar\omega_D)^2} \right] - \cos \left[\frac{2\pi}{(\hbar\omega_D)^2} \left(\mu^2 - \frac{\gamma^2}{4} \right) \right]} \right\}. \quad (\text{S26})$$

From Eqs. (S25a, S26) is straightforward to establish a relation between the oscillating component of the quantum capacitance $C_{q,\text{osc}} = e^2 \partial n_{\text{osc}} / \partial \mu$ and the oscillations of the magnetic susceptibility $\chi_{m,\text{osc}} = \frac{\partial M_{\text{osc}}}{\partial B}$. From Eqs. (S25a-S26), we have that

$$C_{q,\text{osc}} = -\frac{Ne^2}{\pi v_F^2 \hbar^2} \mu \frac{\left\{ e^{-2\pi\gamma\mu/\hbar\omega_D} - \cos \left[\frac{2\pi}{(\hbar\omega_D)^2} \left(\mu^2 - \frac{\gamma^2}{4} \right) \right] \right\} + \gamma/2 \sin \left[\frac{2\pi}{(\hbar\omega_D)^2} \left(\mu^2 - \frac{\gamma^2}{4} \right) \right]}{\cosh \left[\frac{2\pi\gamma\mu}{(\hbar\omega_D)^2} \right] - \cos \left[\frac{2\pi}{(\hbar\omega_D)^2} \left(\mu^2 - \frac{\gamma^2}{4} \right) \right]}, \quad (\text{S27a})$$

$$\chi_{m,\text{osc}} = -\frac{Ne\mu}{4\pi \hbar B} \frac{\left(\mu^2 - \frac{\gamma^2}{4} \right) \left\{ e^{-2\pi\gamma\mu/\hbar\omega_D} - \cos \left[\frac{2\pi}{(\hbar\omega_D)^2} \left(\mu^2 - \frac{\gamma^2}{4} \right) \right] \right\} + \gamma\mu \sin \left[\frac{2\pi}{(\hbar\omega_D)^2} \left(\mu^2 - \frac{\gamma^2}{4} \right) \right]}{(\hbar\omega_D)^2 \left\{ \cosh \left[\frac{2\pi\gamma\mu}{(\hbar\omega_D)^2} \right] - \cos \left[\frac{2\pi}{(\hbar\omega_D)^2} \left(\mu^2 - \frac{\gamma^2}{4} \right) \right] \right\}}, \quad (\text{S27b})$$

which leads to the relation

$$C_{q,\text{osc}} = \frac{\chi_{m,\text{osc}}}{\Gamma(\mu, B)} \quad (\text{S28})$$

with

$$\Gamma(\mu, B) = \frac{\mu^2 - \gamma^2/4}{4B^2 e^2} + \frac{\gamma}{4B^2 e^2} \frac{\mu^2 + \gamma^2/4}{\gamma + 2\mu \sin \left[\frac{2\pi}{(\hbar\omega_D)^2} \left(\mu^2 - \frac{\gamma^2}{4} \right) \right]^{-1} \left\{ \cos \left[\frac{2\pi}{(\hbar\omega_D)^2} \left(\mu^2 - \frac{\gamma^2}{4} \right) \right] - \exp \left[\frac{2\pi\gamma\mu}{(\hbar\omega_D)^2} \right] \right\}}. \quad (\text{S29})$$

Here for $\mu \gg \gamma$, we obtain

$$\Gamma(\mu, B) = \left(\frac{\mu}{2eB} \right)^2. \quad (\text{S30})$$

Neglecting the small oscillations of the chemical potential, it is therefore clear that the dips in the dependence of the mechanical resonant frequency ω_n as a function of B , which were previously been interpreted in terms of quantum capacitance oscillations, can equivalently be interpreted in terms of oscillations of the magnetic susceptibility χ_m (de Haas – van Alphen effect).

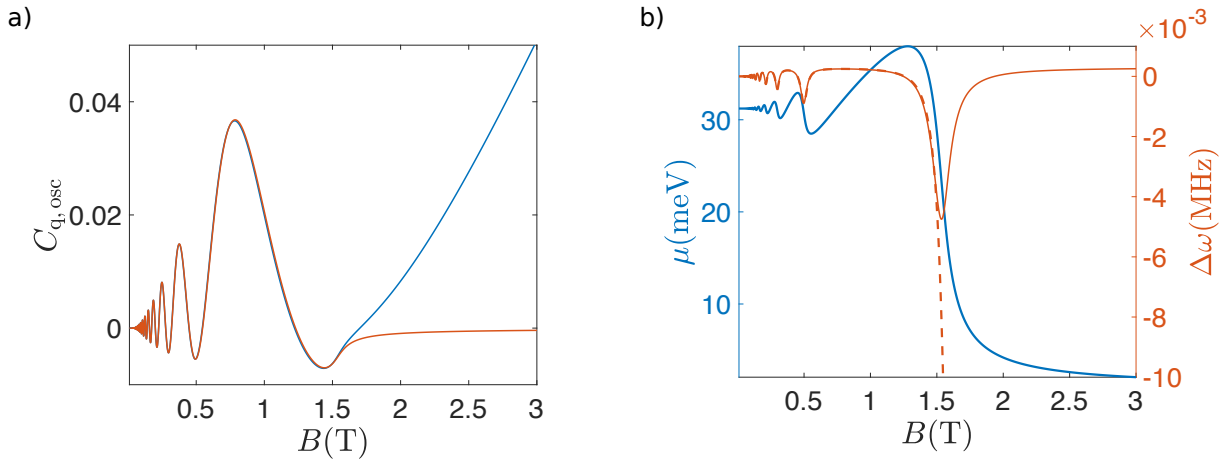


FIG. S4. a) Value of $C_{q,osc}$ calculated through the relation $C_{q,osc} = \frac{\chi_{m,osc}}{\Gamma(\mu,B)}$, for the value of $\Gamma(\mu,B)$ given in equation (S29) (blue line), and for the zeroth-order expansion in γ (equation (S30), red line). b) Corresponding plot of the frequency shift. Exact value of $\Gamma(\mu,B)$ (continuous line), zeroth-order expansion in γ (dotted line). All parameters are the ones used for the data fit of device B1.5.

* These two authors contributed equally

† francesco.massel@usn.no

- [1] H. B. Callen, *Thermodynamics and an Introduction to Thermostatistics*, John Wiley & Sons (John Wiley & Sons, 2006).
- [2] G. L. Yu, R. Jalil, B. Belle, A. S. Mayorov, P. Blake, F. Schedin, S. V. Morozov, L. A. Ponomarenko, F. Chiappini, S. Wiedmann, et al., *Proceedings of the National Academy of Sciences* **110**, 3282 (2013).
- [3] G. A. Steele, A. K. Hüttel, B. Witkamp, M. Poot, H. B. Meerwaldt, L. P. Kouwenhoven, and H. S. J. van der Zant, *Science* **325**, 1103 (2009).
- [4] B. Lassagne, Y. Tarakanov, J. Kinaret, D. Garcia-Sanchez, and A. Bachtold, *Science* **325**, 1107 (2009).
- [5] J. Atalaya, A. Isacsson, and J. M. Kinaret, *Nano Letters* **8**, 4196 (2008).
- [6] C. Chen, V. V. Deshpande, M. Koshino, S. Lee, A. Gondarenko, A. H. MacDonald, P. Kim, and J. Hone, *Nature Physics* **12**, 240 (2015).
- [7] S. G. Sharapov, V. P. Gusynin, and H. Beck, *Phys. Rev. B* **69**, 075104 (2004).